

## Seismicity Properties of the Chain Transform Fault Inferred Using Data From the PI-LAB Experiment

K. Leptokaropoulos<sup>1,2</sup> , C. A. Rychert<sup>1,3</sup> , N. Harmon<sup>1,3</sup> , and J. M. Kendall<sup>4</sup> 

<sup>1</sup>Ocean and Earth Science, University of Southampton, Southampton, UK, <sup>2</sup>The MathWorks, Cambridge, UK, <sup>3</sup>Geology and Geophysics, Woods Hole Oceanographic Institution, Woods Hole, MA, USA, <sup>4</sup>Department of Earth Sciences, University of Oxford, Oxford, UK

### Key Points:

- Segmentation along Chain transform fault (Mid-Atlantic Ocean) is studied by means of seismicity cluster analysis and geophysical data
- Chain demonstrates lateral heterogeneity with high moment-release patches interrupted by segments with abundant but small magnitude events
- Spatiotemporal variations of seismicity are possibly manifested by variable hydrothermal circulation and alteration

### Supporting Information:

Supporting Information may be found in the online version of this article.

### Correspondence to:

K. Leptokaropoulos,  
K.Leptokaropoulos@soton.ac.uk

### Citation:

Leptokaropoulos, K., Rychert, C. A., Harmon, N., & Kendall, J. M. (2023). Seismicity properties of the Chain transform fault inferred using data from the PI-LAB experiment. *Journal of Geophysical Research: Solid Earth*, 128, e2022JB024804. <https://doi.org/10.1029/2022JB024804>

Received 19 MAY 2022

Accepted 16 FEB 2023

### Author Contributions:

**Conceptualization:** K. Leptokaropoulos, C. A. Rychert, N. Harmon

**Data curation:** K. Leptokaropoulos

**Formal analysis:** K. Leptokaropoulos

**Funding acquisition:** C. A. Rychert

**Investigation:** K. Leptokaropoulos, C. A. Rychert

**Methodology:** K. Leptokaropoulos, N. Harmon, J. M. Kendall

**Project Administration:** C. A. Rychert

**Resources:** C. A. Rychert, N. Harmon, J. M. Kendall

© 2023. The Authors.

This is an open access article under the terms of the [Creative Commons Attribution License](#), which permits use, distribution and reproduction in any medium, provided the original work is properly cited.

**Abstract** Oceanic transform faults are intriguing in that they do not produce earthquakes as large as might be expected given their dimensions. We use 1-year of local seismicity (370 events above  $M_C = 2.3$ ) recorded on an array of ocean bottom seismometers (OBSs) and geophysical data to study the seismotectonic properties of the Chain transform, located in the equatorial Mid-Atlantic. We extend our analysis back in time by considering stronger earthquakes ( $M_W \geq 5.0$ ) from global catalogs. We divide Chain into three areas (east, central, and west) based on historical event distribution, morphology, and multidimensional OBS seismicity cluster analysis. Seismic activity recorded by the OBS is the highest at the eastern area of Chain where there is a lozenge-shaped topographic high, a negative rMBA gravity anomaly, and only a few historical  $M_W \geq 5.5$  events. OBS seismicity rates are lower in the western and central areas. However, these areas accommodate the majority of seismic moment release, as inferred from both OBS and historical data. Higher  $b$ -values are significantly correlated with lower rMBA and with shallower bathymetry, potentially related to thickened crust. Our results suggest high lateral heterogeneity along Chain. Patches with moderate to low OBS seismicity rates that occasionally host  $M_W \geq 6.0$  earthquakes are interrupted by segments with abundant OBS activity but few historical events with  $5.5 \leq M_W < 6.0$ . This segmentation is possibly due to variable fluid circulation and alteration, which may also change in time.

**Plain Language Summary** Oceanic transform faults (TFs) typically host earthquakes much smaller than expected based on their total seismogenic area. We study the seismotectonic properties of the Chain TF by combining 1-year of seismicity recorded by an ocean bottom seismometer (OBS) array with geophysical data (bathymetry, tidal height, gravity anomalies). We supplement our analysis with strong historical earthquakes ( $M \geq 5.0$ ) from global catalogs. Our analysis divides Chain into three areas: The east area is characterized by the highest OBS seismicity rates, negative gravity anomalies, large topographic highs, and few historical events with  $5.5 \leq M < 6.0$ . The west and central areas demonstrate lower OBS seismicity rates. However, they occasionally produce  $M \geq 6.0$ , being responsible for most of the total seismic energy release. Higher numbers of stronger events occur in areas with negative gravity anomalies and shallower water depths. Our results suggest high lateral heterogeneity along Chain, with alternating seismic and aseismic patches, variable crustal thickness, different degrees of hydrothermal circulation/alteration, and potentially time-dependent behavior.

## 1. Introduction

Oceanic transform faults (TFs) are steeply dipping fault segments of young oceanic lithosphere bounded between mid-ocean ridge spreading centers. They are thought to have a simple structure in comparison to their continental counterparts given that the composition of the ocean crust and upper mantle is relatively homogenous and generally lacks the complex lateral variability commonly evident in the continental crust (e.g., Behn et al., 2007; Wolfson-Schwehr & Boettcher, 2019). Along the axis of an oceanic TF, lithospheres of different age, and thus with different thermal and mechanical properties, interact.

Ridge-transform plate boundaries may also enhance hydrothermal circulation, substantially impacting geophysical, geochemical, and biological processes (e.g., Hensen et al., 2019). Such phenomena are plausibly very typical in marine transform systems. TFs themselves may exhibit fault zone damage which can also contribute to hydrothermal circulation and alteration along the transform valley (Froment et al., 2014; Kohli et al., 2021). Exposure of altered peridotites and gabbro at detachment faults along fracture zones and core complexes (Blackman

**Software:** K. Leptokaropoulos, N. Harmon  
**Supervision:** C. A. Rychert, N. Harmon  
**Validation:** K. Leptokaropoulos  
**Visualization:** K. Leptokaropoulos  
**Writing – original draft:** K. Leptokaropoulos, C. A. Rychert, N. Harmon  
**Writing – review & editing:** K. Leptokaropoulos, C. A. Rychert, N. Harmon, J. M. Kendall

et al., 1998) show that these locations promote serpentinization, and therefore play an important role in potentially altering the frictional properties of the lithosphere.

Most of the seismicity within the Mid Atlantic Ridge (MAR) is concentrated along ridge spreading centers and TFs, with the latter typically hosting larger magnitude events (with  $M_w$  up to around 7.0) and having unusually high stress drops and apparent stress compared to the global average for TFs (Scholz, 2019). It has been, nevertheless, continuously acknowledged (e.g., Brune, 1968) that oceanic TFs accommodate much fewer and smaller events (i.e., less seismic moment release) than would be anticipated considering the global scaling relationships between fault dimensions and earthquake size (e.g., Wells & Coppersmith, 1994). This is because slip along TFs takes place by both seismic (earthquakes) and aseismic (creeping) processes, with most of the slip occurring either aseismically or released by microseismicity and earthquake swarms in the mantle (Boettcher & Jordan, 2004; Kuna et al., 2019; Roland et al., 2010). The estimated low seismic coupling at TFs has led to the idea that stresses in oceanic TFs are primarily driven by slow transients, with earthquakes (fast ruptures) being just “aftershocks” of the creeping or silent events (Boettcher & Jordan, 2004). Although there is a great variation of seismic coupling among marine TFs (Wolfson-Schwehr & Boettcher, 2019), the work of Boettcher and Jordan (2004) found a global mean of coupling coefficient  $\sim 15\%$  along oceanic TFs. This result came after binning by thermal area and averaging, assuming the classical brittle-ductile transition at the 600°C isotherm prediction from thermal models (Abercrombie & Ekström, 2001; Behn et al., 2007). The value of 15% may be a maximum estimate if the brittle-ductile transition occurs deeper, as earthquakes at TF have been located at deeper depths than the predicted brittle-ductile transition (Kuna et al., 2019; Marjanović et al., 2020; McGuire et al., 2012; Schlaphorst et al., 2022). These depths could be owing to greater amounts of hydrothermal alteration than predicted by rheological models (Roland et al., 2010). Alternatively, ruptures at higher temperatures might be expected at transforms owing to the relatively high strain rates (Molnar, 2020). Exhumed mylonites suggest that brittle and ductile deformation can both occur anywhere between 300°C and 1000°C (Kohli et al., 2021).

Our current knowledge of the structure and dynamics of oceanic TFs is limited by their remote location, hundreds or thousands of kilometers away from the continents, where seismometers are typically installed. Most of the available seismicity data comes from teleseismic events in catalogs with high magnitudes of completeness ( $M_c > \sim 5.0$ ). Such studies, although important (e.g., Engeln et al., 1986), offer a limited insight into the seismotectonic processes of mid-ocean ridges and adjacent TFs. Some high-resolution analyses have been conducted using regional seismic networks (e.g., Braunmiller & Nabelek, 2008) revealing TF segmentation in relative detail. Even higher resolution constraints on seismicity in these remote areas can be facilitated by specifically targeted deployment of instruments, including networks of ocean bottom seismometers (OBSs).

One such deployment was carried out from March 2016 to March 2017 at the equatorial MAR. Chain TF as well as the adjacent spreading centers and fracture zones were comprehensively studied under the framework of the PI-LAB (Passive Imaging of the Lithosphere-Asthenosphere Boundary) and the EURO-LAB (Experiment to Unearth the Rheological Lithosphere-Asthenosphere Boundary) projects. In addition to deploying 39 OBSs and 39 ocean bottom magnetotelluric instruments, multibeam bathymetry and back scatter imagery, gravity and magnetic data were collected (Harmon et al., 2018). The experiment was designed to image the lithosphere and the asthenosphere near a slow spreading center using a range of methodologies, sensitivities, and resolutions (Harmon et al., 2020, 2021; Rychert et al., 2021; Saikia et al., 2021b; S. Wang et al., 2019, 2020). The goal was to determine what makes a plate “plate-like” (Fischer et al., 2010, 2020; Rychert et al., 2020). The data from the experiment also provided an opportunity to study a range of other phenomena, including, for instance, constraining local sediment properties (Agius et al., 2018; Saikia et al., 2020), imaging the mantle transition zone (Agius et al., 2021), determining 1D oceanic attenuation structure (Saikia et al., 2021a), tracking infragravity waves in the ocean (Bogiatzis et al., 2020), developing better corrections to improve normal mode measurements for seafloor data (Harmon et al., 2022), tidal triggering at the MAR (Leptokaropoulos et al., 2021), and TF seismicity on the nearby Romanche (Hicks et al., 2020) and the Chain TFs. Our study focuses on the Chain TF, which is characterized by a narrow 0–20 Myr old rupture zone, stretching over 300 km in roughly the east-west direction between two ridge spreading axes, slipping at a full spreading rate of  $\sim 30$  mm/yr. Within the active fault zone, there are four lozenge shaped shallow bathymetric features, with en échelon fault scarps that were previously mapped and investigated in the work of Harmon et al. (2018; Figure 1). These features show evidence for reverse faulting in the sediments near the scarps, suggesting that these features are transpressional in nature. The features are interpreted as positive flower structures (Harding, 1985). The largest flower structure is located in the eastern Chain TF and is associated with a negative residual mantle Bouguer anomaly (rMBA) (Harmon et al., 2018). We

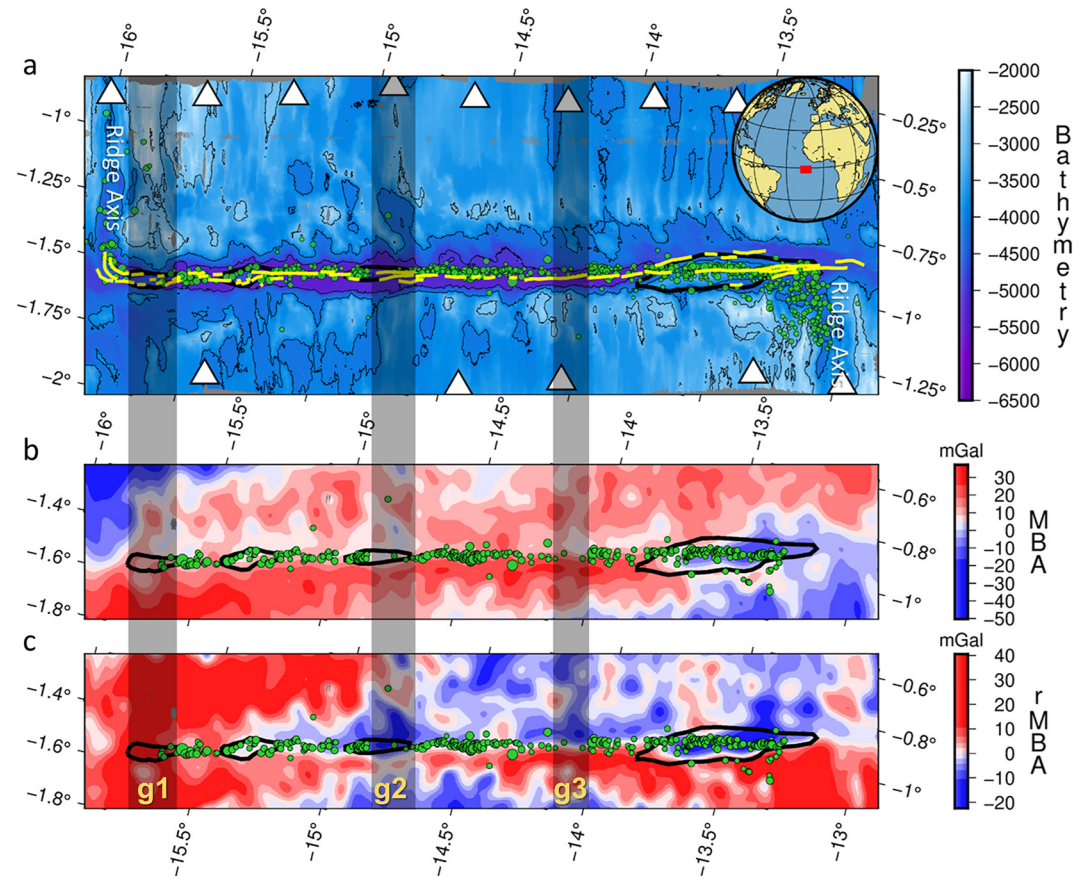


**Figure 1.** Geophysical features of Chain transform fault (TF) from Harmon et al. (2018) and all local seismicity located by Schlaphorst et al. (2022) presented as green circles. The locations of the closest ocean bottom seismometer (OBS) stations are represented by white triangles. (a) Bathymetric map of the study area with main faults (yellow curves) and flower structures (black curves). Bathymetry also delineates the ridge spreading centers that bound Chain, at the upper left and lower right parts of panel (a). The inset map at the upper right corner shows the location of Chain, marked by the red box. (b) Mantle Bouguer anomaly (MBA) in the study area. (c) Residual mantle Bouguer anomaly (rMBA) in the study area. Seismicity along Chain above completeness magnitude ( $M_c = 2.3$ ), which was used for the analysis in this study is depicted as green circles in (b) and (c). The vertical shaded bars mark the location of the three OBS seismicity gaps (g1, g2, g3), discussed in the text.

refer to this structure as the eastern large flower structure (ELFS). The observed gravity anomaly at ELFS can be explained either by thicker crust or highly altered or damaged material (Harmon et al., 2018).

In this study, we use the 1-year seismicity catalog presented in the work of Schlaphorst et al. (2022) and additional marine geophysical data gathered by the PI-LAB experiment (Harmon et al., 2018), focusing on the properties of seismicity of the Chain TF (Figure 1). We investigate the space, time, and size distribution of seismicity along Chain TF and its connection to gravity anomalies and bathymetrical features. We perform cluster analysis in multidimensional phase space, consisting of various seismic and geophysical parameters. We extend our analysis in time by considering strong events ( $M_w \geq 5.0$ ) from the Global Centroid Moment Tensor catalog (GCMT, Ekström et al., 2012) and the corresponding epicentral locations from the International Seismological Center (ISC). We extract information on the lithospheric structure and physical properties of the TFs by evaluating seismicity distribution and  $b$ -values, identifying seismicity gaps, and integrating our results with previous findings.

## 2. Materials and Methods

### 2.1. Seismicity Catalog

The seismicity catalog compiled by Schlaphorst et al. (2022) contains 972 events, 812 of which are located within the area surrounded by the OBS network, which contains the Chain TF and the adjacent ridge spreading



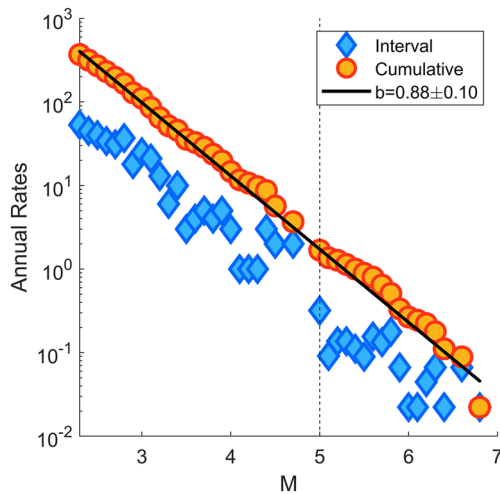


**Figure 2.** Interval (blue) and cumulative (yellow) annual frequency versus magnitude for Chain transform fault (TF). Data between 1976 and 2021 come from Global Centroid Moment Tensor (GCMT) and data between March 2016 and March 2017 come from the ocean bottom seismometer (OBS) network (see text for temporal completeness levels). The solid black line indicates  $b = 0.88$ , whereas the vertical dashed line shows the transition from OBS (left) to GCMT data (right), around  $M = 5.0$ .

seismicity along the MAR (30°S–30°N) aligns well with the main active ridge or TF bathymetry, although a small number of lower magnitude events might be related to the secondary bathymetric features. Therefore, we proceed with our analysis under the assumption that all  $M_w \geq 6.0$  earthquakes considered in the study occurred along the Chain TF. For the most recent events that occurred after 1993, we use the relocated epicenters from Shi et al. (2021). Events before this time also have higher location uncertainties.

We integrated our local catalog with the available historical data (Figure 2). In doing so, we make the following assumptions and assess their validity:

1. The  $M_L$  from the OBS catalog scales linearly with the  $M_w$  from GCMT, with  $M_L \sim M_w$ .
2. Magnitude distribution obeys the same GR law for large ( $M_w \geq 5.0$ , GCMT) as well as for smaller ( $2.3 \leq M_L \leq 5.0$ , OBS) earthquakes.
3. The overall magnitude distribution remains similar (sufficiently stable) from 1976 to 2021.

The completeness magnitude of the GCMT catalog for the study area is determined as a function of time. The Anderson Darling Test (Leptokaropoulos, 2020; Marsaglia & Marsaglia, 2004; Text S2 in Supporting Information S1) is performed in various time windows and establishes that  $M_c = 5.4$  for 1976–2002 and  $M_c = 5.0$  starting in 2004. This changing point is consistent with the work of Ekström et al. (2012), which reports that significant enhancements were introduced in the GCMT processing starting in 2004. A total of 53 events from GCMT, satisfy the aforementioned conditions. The annual rates of events considering these data are evaluated and then are merged with the OBS catalog (which corresponds directly to annual rates). There are four common events in the two catalogs, which have similar magnitudes (0.0–0.3 units difference). For these events we keep the  $M_L$  from the OBS catalog. In addition, the mean absolute difference in the longitude between OBS and teleseismic data (as reported from the ISC) for these four events is 0.05°, whereas the corresponding mean latitude difference is 0.18°. This suggests that although the ISC epicentral locations have naturally larger uncertainties than OBS solutions, the longitude is sufficiently estimated and can be used as a good first order approximation. However, to have more precise locations for the along-strike variation of large events recorded since 1993 in our following analysis, we use the relocated catalog of Shi et al. (2021).

The annual event frequency of the merged catalog is shown in Figure 2. Overall, the data seem to obey the GR law with no visible changes in slope around  $M = 5.0$ , that is, the transition from the OBS to the GCMT catalog. The repeated median (RM) technique (Amorèse et al., 2010; Text S2 in Supporting Information S1)

centers (Figure 1b). To focus on the TF seismicity, we discard the events that occurred unequivocally at the ridge segments and at the inside corners, based on their proximity to the spreading axis (10 km) and the available focal mechanisms. After this selection, 626 events remain along the Chain transform valley from 13 March 2016 to 15 March 2017, characterized by a local magnitude ( $M_L$ ) range between 1.1 and 5.4. The epicentral coordinates of these events are sufficiently constrained with median lateral uncertainties of 2.5 km. The vertical uncertainties are larger (median 18 km) with several events having uncertainties greater than 20 km. Given the large depth uncertainties for some of the events considered here, depth is not included as a parameter in the cluster analysis (see Section 2.2). For 114 of these events focal mechanism solutions were derived, with 89 of them having good quality and depth determination, with mean vertical uncertainties of 6 km. Further analysis of those earthquakes, including their focal mechanisms and depths (Text S1 in Supporting Information S1), can be found in the work of Schlaphorst et al. (2022). The completeness magnitude ( $M_c$ ) of our catalog is 2.3 (Text S2 in Supporting Information S1).

The OBS network provides well-located seismic events but only covers a limited time period and does not include events larger than  $M_w \sim 5.5$ . To obtain better insights on how seismicity along Chain evolves within timescales of the order of decades, we use GCMT data, considering events with  $M_w \geq 5.0$  after 1976. For the events that occurred before 1976, there are considerable uncertainties in the epicentral locations (larger in latitude than in longitude), both relative and absolute. Pan et al. (2002) demonstrate that

returns  $b = 0.88 \pm 0.10$  for the merged catalog, which is close to the corresponding value from the OBS catalog,  $b_{\text{obs}} = 0.83 \pm 0.09$ . This provides an indication that  $M_L \sim M_W$ , and thus, the first two assumptions can be considered valid. There is a deficit of strong events at  $M_W > \sim 6.5$ , which is typical for oceanic TFs (e.g., Boettcher & Jordan, 2004). Yet, the third assumption can be also considered valid, since the 45 year-period from which we took the data should be representative of a complete seismic cycle, even in slow spreading oceanic ridge TFs (e.g., Aderhold & Abercrombie, 2016; Boettcher & McGuire, 2009).

## 2.2. Cluster Analysis

Every seismic event can be represented by a point in a multidimensional space, quantified by a vector of values corresponding to parameters such as origin time, focal coordinates, magnitude, source dimensions, moment tensor components, etc. Studies of earthquake clustering typically consider distances between such points in multi-parameter spaces. However, the metric in such spaces cannot be readily defined, since different parameters demonstrate diverse ranges, distributions, and scalings. Transformation to Equivalent Dimension (ED) is a solution to this metric problem proposed by Lasocki (2014) based on the concept of probabilistic equivalence of continuous parameters. Following this approach, the lengths of parameter intervals are equivalent if the probability for earthquakes to take values from either interval is the same. Earthquake parameter distributions, which, in general, lack functional forms, are assessed using the nonparametric (data-driven) kernel estimation (Silverman, 1986).

Let a seismic event be described by a set of continuous parameters  $X_i$  ( $X_1, \dots, X_n$ ), with cumulative distribution functions (CDF) of  $F_{X_1}, \dots, F_{X_n}$ , respectively (Figure S4 in Supporting Information S1). The ED of  $X_i$  is  $U_i = F_{X_i}(X_i)$ , with  $U_i$  uniformly distributed within  $[0, 1]$ . Each event is now parameterized by the  $U(U_1, \dots, U_n)$  vector in a  $n$ -dimensional space where the metric is Euclidean, such that the distance,  $D$ , between two events  $A$  and  $B$  can be defined as:

$$D(A, B) = \sqrt{\sum_{i=1}^n (U_i(A) - U_i(B))^2} \quad (1)$$

After the transformation of seismic parameters into their ED, earthquake clustering is performed, with parameters chosen to identify spatial clusters (segmentation) along the Chain TF. In such a way, we investigate the potential association among events by considering additional properties than just their locations along the transform. We establish clusters in multidimensional space considering their linkage distance as derived by the hierarchical clustering approach introduced in the work of Ward (1963), which creates branches of interconnection among the points (earthquakes). This technique forms groups of mutually exclusive clusters until all clusters eventually join one group (event population). The degree of connection among individual events and the clusters that they gradually form is represented by a dendrogram. The linkage distance between clusters 1 and 2,  $d_{12}$  is specified as the average distance between all pairs of events in any of the clusters:

$$d_{12} = \frac{1}{mn} \sum_{i=1}^m \sum_{j=1}^n d(X_i, Y_j) \quad (2)$$

where  $X_1, \dots, X_i$  are observations from cluster 1,  $Y_1, \dots, Y_j$  are observations from cluster 2,  $d(X_i, Y_j)$  is the distance between a subject with observation vector  $X$  and a subject with observation vector  $Y$ , and  $d_{12}$  measures the degree of connection between clusters 1 and 2. Note that all  $X_i$  and  $Y_j$  values are in ED. The smallest linkage distance defines when events/clusters are joined, as described in the Ward (1963) method. Cluster analysis depends somewhat on the chosen method (Figure S5 in Supporting Information S1), parameter selection, number of derived clusters (Figure S6 in Supporting Information S1), and selected degree of connection (Linkage distance cut-off). The number of clusters can be determined based on the desired linkage distance cut-off, selected after considering a trade-off between the size of clusters and their corresponding degree of interconnection. We perform cluster analysis in multidimensional space considering the following earthquake parameters (units in brackets):

- Longitude [°N]
- Latitude [°E]
- Local magnitude
- Tidal height [m]

- Mantle Bouguer Anomaly (MBA) [mGal]
- Residual Mantle Bouguer Anomaly (rMBA) [mGal]
- Bathymetry [m]

These parameters were chosen as they are either directly related to the earthquake (longitude, latitude, local magnitude), predictable changes in hydrostatic stress along the fault (tidal height), or related to variations in fault crustal structure (MBA, rMBA, Bathymetry). The spatial resolution for all the parameters is two decimals except the magnitude (one decimal). The CDF of these parameters (before their transformation to equivalent dimensions) are shown in Figure S4 in Supporting Information S1. The latter three parameter values, originally estimated by Harmon et al. (2018) in a dense grid covering the study area, are assigned to each earthquake by nearest neighbor interpolation at the event epicenters. The epicentral locations and local magnitudes come from Schlaphorst et al. (2022). The ocean tides are calculated by the SPOTL software (Agnew, 1997) considering the global ocean tide model TPX072.2010, produced by Oregon State University (Egbert & Erofeeva, 2002). The tidal constituents M2, N2, S2, K2, K1, P1, O1, and Q1 are considered to calculate the predicted tidal heights (Agnew, 1997 and references therein) at the epicentral coordinates of each event for a 13 hr time span, centered at each event's occurrence time, with a time step for subsequent calculations equal to 72 s. By doing this we ensure that a complete semidiurnal tidal cycle ( $\sim 12$  hr 25 min) is covered and a tidal phase within the cycle can be assigned to each event (Leptokaropoulos et al., 2021). We define the tidal phase,  $\phi$ , relative to the low tide. In other words,  $0^\circ$  corresponds to the minimum water level,  $\pm 90^\circ$  correspond to zero tidal height, whereas  $+180^\circ$  and  $-180^\circ$  correspond to the subsequent and preceding high tides (maximum water level), respectively. The preference for a specific phase range is evaluated by the Schuster test (see Text S3 in Supporting Information S1).

### 3. Results

#### 3.1. OBS Seismicity Cluster Analysis

The cluster analysis in the seven-parameter space shows that spatial clusters are formed at different linkage distances, with four main clusters indicated in Figure 3. In our study we select a high-level division into two major clusters based on the dendrogram in Figure 3 (eastern—ELFS and rest of Chain). We further divide the rest of Chain seismicity into two segments (central and west) based on morphology (west has three flower structures, central has none) which is in good agreement with the cluster analysis results considering three and four clusters (Figure 3, Figures S6–S18 in Supporting Information S1). Although there is a small spatial overlap among the clusters, it is evident that Cluster 1 (108 events, blue) occupies the western part of Chain TF, Cluster 2 (126 events, orange) mostly covers the central part of the transform valley, whereas Cluster 3 (118 events, yellow) and Cluster 4 (18 events, purple) are located at the eastern part of Chain. Cluster 3 almost exclusively includes events within the ELFS, whereas Cluster 4 is located at the eastern tips and south of the ELFS. Due to the small size of Cluster 4 (18 events) and its spatial proximity to Cluster 3, we decided to merge these two clusters, hereinafter referred to as Cluster 3/4. The inset at the bottom of Figure 3 shows the interrelation dendrogram formed by the 370 events with  $M_L \geq 2.3$ , comprising the complete data obtained from the OBS network. Note, however, that the dendrogram indicates that Cluster 1 and Cluster 2 are more closely linked with each other in the 7-dimension space than Cluster 3 and Cluster 4. In addition, some of the Cluster 4 events are located at the core complex rather than at the transform. For this reason, we also present the results for Cluster 3 alone, simply discarding the 18 events of Cluster 4 from the analysis, although the results remain essentially similar (Table 1). In the end, we prefer three clusters, based on our testing of choice of parameters, as well as the fact that they correspond to the changes in morphology along strike of the Chain (i.e., presence or absence of flower structures). We proceed in our analysis of these three segments western, central, and eastern.

We apply and demonstrate the results in the seven-parameter space (Figure 4; Figure S7 in Supporting Information S1). However, to investigate the stability of the clustering results, we perform various combinations of the seven selected parameters. First, we try the seven 6-parameter combinations, that is, removing one parameter each time. In all these cases (Figures S8–S14 in Supporting Information S1), the clustering at the ELFS is prominent. The division of seismicity in the western and central segments is apparent when disregarding  $M_L$  (Figure S10 in Supporting Information S1), rMBA (Figure S12 in Supporting Information S1), bathymetry (Figure S13 in Supporting Information S1), and ocean tides (Figure S14 in Supporting Information S1).

We further apply four-parameter and five-parameter trials ( $35 + 21 = 56$  combinations). Some examples are shown in Figures S15–S17 in Supporting Information S1. We verify a strong clustering at the ELFS in all cases, even when the longitude and latitude are discarded (Figure S15 in Supporting Information S1). This shows that

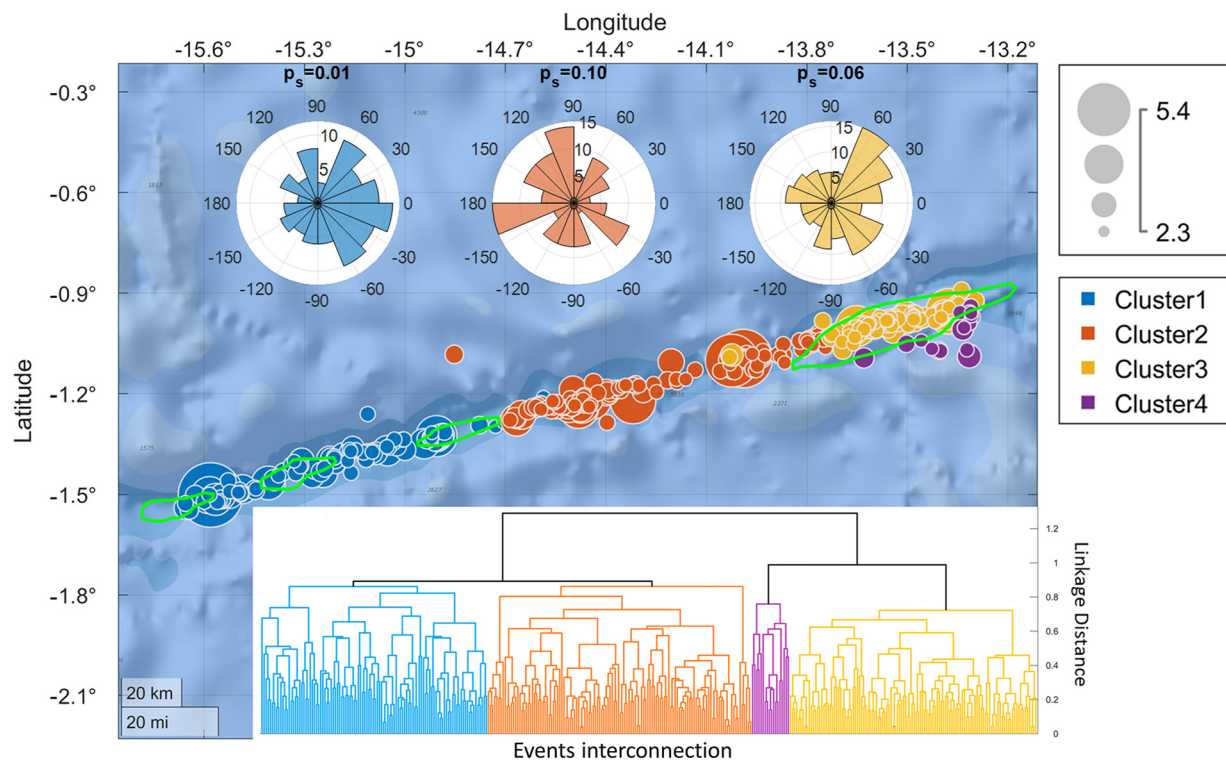


**Figure 3.** Spatial distribution of the four major clusters derived by the hierarchical cluster analysis. The inset at the lower part of the figure presents the dendrogram showing the interconnection among the earthquakes, ultimately forming a tree. The lower the branches meet with each other the stronger the clustering. Linkage distance is indicated at the y-axis on the right. The colors in the dendrogram correspond to the colors of the clusters in the map and the circles' size is proportional to the event magnitudes ( $2.3 \leq M_L \leq 5.4$ ). The polar histograms at the top of the figure show the tidal phase distribution for each cluster (from left to right, Cluster 1, Cluster 2, Cluster 3, indicated by the respective colors) and the corresponding Schuster test  $p$ -value,  $p_s$ . The green curves delineate the four positive flower structures.

seismicity at ELFS has unique properties in terms of the selected parameters and can be clearly separated from the rest of Chain. On the other hand, not all parameters are equally important in separating the remaining seismicity to the west of the ELFS. When either latitude (Figure S8 in Supporting Information S1), longitude (Figure S9 in Supporting Information S1), or MBA (Figure S11 in Supporting Information S1) is disregarded the separation between the western and central segment collapses. This indicates that these three parameters play the most important role in segmentation along Chain. Cluster analysis in the three-dimensional space (latitude, longitude, and MBA, Figure S18 in Supporting Information S1) yields a division into three segments: west, central, and east.

Table 1 shows an overview of seismic and geophysical parameters that characterize the three dominant clusters. The distributions of magnitudes, bathymetry, MBA, and rMBA are shown in Figure 4. Figure 4a shows the cumulative magnitude distribution of the three clusters. Cluster 1 and Cluster 3 have similar magnitude distributions, with

**Table 1**  
Summary of the Properties of the Main Clusters Derived by Multidimensional Cluster Analysis (Shown in Figure 3)

Cluster ID	$N$	$b$ -value	$M_0$ ( $\times 10^{17}$ Nm)	Bathymetry (m)	MBA (mgal)	rMBA (mgal)	Tidal height (cm)	$p_s$
Cl. 1	108	$0.91 \pm 0.12$	1.60	$5,327 \pm 255$	$10.7 \pm 2.7$	$-0.3 \pm 4.9$	$-17.1 \pm 33.3$	0.01
Cl. 2	126	$0.71 \pm 0.13$	1.40	$5,105 \pm 274$	$14.4 \pm 3.1$	$-0.2 \pm 3.3$	$9.7 \pm 30.0$	0.10
Cl. 3	118	$0.97 \pm 0.18$	0.25	$3,806 \pm 373$	$-5.2 \pm 6.0$	$-9.6 \pm 3.1$	$-12.3 \pm 3.1$	0.06
Cl. 3/4	136	$0.95 \pm 0.18$	0.26	$3,847 \pm 433$	$-4.1 \pm 6.5$	$-7.1 \pm 7.4$	$-13.6 \pm 3.0$	0.06

*Note.* The columns indicate subsequently: the Cluster ID; the number of events,  $N$ ; the  $b$ -value; the total seismic moment release,  $M_0$ ; the mean bathymetry; the mean MBA; the mean rMBA; the median tidal height, with negative and positive values corresponding to low and high tides, respectively; the  $p$ -value of the Schuster test,  $p_s$ . The numbers following the  $\pm$  symbol, indicate one standard deviation.



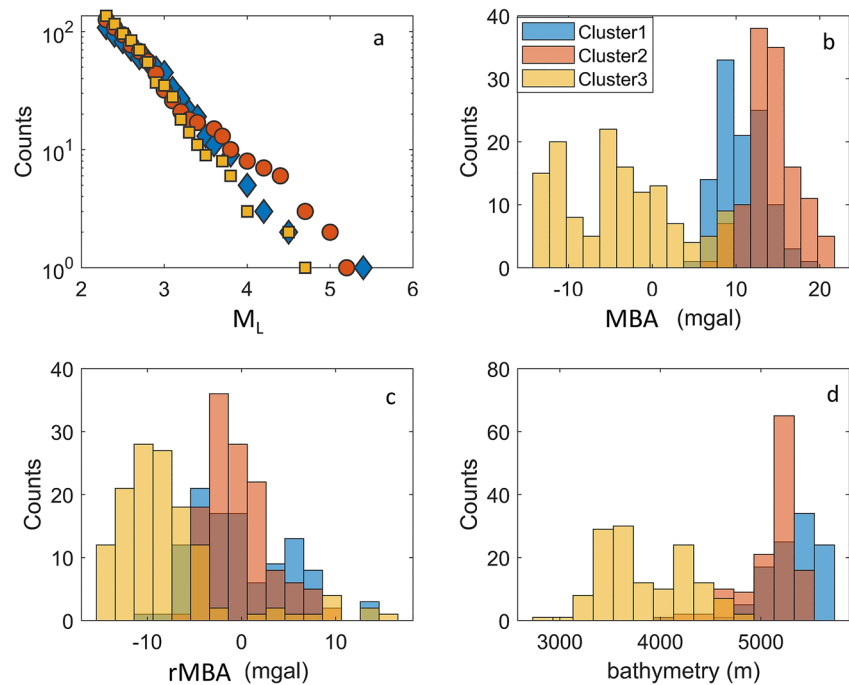


**Figure 4.** Value ranges of each parameter for Cluster 1 (blue), Cluster 2 (red), and Cluster 3/4 (yellow). The corresponding parameters are labeled in the  $x$ -axis: (a)  $M_L$ , (b) MBA, (c) rMBA, and (d) bathymetry. Note that the cluster analysis has been carried out in the equivalent dimensions, whereas these histograms represent the values in the original dimensions.

Cluster 1 including more events with  $M_L > 3.0$  than Cluster 3. In addition, the largest event in the catalog ( $M_L = 5.4$ ) belongs to Cluster 1, leading to a lower  $b = 0.91 \pm 0.15$ , in comparison with  $b = 0.97 \pm 0.18$  estimated for Cluster 3, although the two are not statistically different from one another. On the other hand, Cluster 2 contains a considerably higher number of larger events ( $M_L > 3.5$ ), compared to the other two clusters, evident by a characteristic change of slope in the cumulative distribution above this magnitude threshold. Consequently, the  $b$ -value of Cluster 2 equals  $0.71 \pm 0.13$ , considerably lower than the  $b$ -values of Clusters 1 and 3. However, the total seismic moment release,  $M_0$ , (derived as in Hanks & Kanamori, 1979), is roughly equal for Cluster 1 and Cluster 2 ( $\sim 1.5 \times 10^{17}$  Nm), being approximately six times higher than the  $M_0$  released by Cluster 3/4. This means that although seismicity rates are much higher at the ELFS, this part of Chain contributes only a small proportion of the total seismically released energy. The closer connection between Cluster 1 and Cluster 2 in the seven-dimensional space, compared to Cluster 3/4, is evident by the distributions of MBA, rMBA, and bathymetry values (Table 1; Figures 4b–4d, respectively). Events belonging to Cluster 3/4 have the lowest values in all three aforementioned parameters, generally corresponding to negative MBA and rMBA values, and a mean ocean depth of 3,800–3,850 m, depending on whether the events from Cluster 4 are included. Clusters 1 and 2 are associated with deeper bathymetry ( $\sim 5,300$  m and  $5,100$  m, respectively), whereas they both have positive mean MBA, somewhat higher for Cluster 2 (Table 1). Both Clusters 1 and 2 show close to zero mean rMBA values (Table 1). However, Cluster 1 has a bimodal distribution with two local maxima around  $-5$  mgal and  $+5$  mgal (Figure 4c). Finally, the tidal phase diagrams are shown in the upper inset of Figure 3. The tidal height associated with the occurrence time of the events, is shifted toward low tides ( $0^\circ$ ) for Cluster 1 and Cluster 3, and slightly shifted toward high tides for Cluster 2 ( $180^\circ$ ) (Table 1). This indicates a minor preference for events occurring at low tides (tidal phase between  $-90^\circ$  and  $90^\circ$ ) closer to the two edges of Chain.

We further investigate the magnitude distribution dependence on individual parameters. In doing so, we consider MBA, rMBA, bathymetry, and tidal height values, sorted in an ascending order, and then we calculate  $b$ -values and their standard error with the RM technique. After performing calculations for different sliding windows consisting of 50, 75, 100, and 125 events, advancing by 1 event, we obtained similar results. We therefore present the results for 100-event windows (Figure 5). Figure 5a shows  $b$ -value fluctuations with MBA. Apart from some relatively elevated  $b$ -values for  $MBA < -3$  mgal, no remarkable variations are evident throughout the MBA range. Negative MBA values are almost exclusively met beneath the ELFS, where the shallowest bathymetry is observed. The rMBA plot shows two distinct domains divided at  $rMBA \sim -3$  mgal (Figure 5b). Event windows with  $rMBA < -3$  mgal



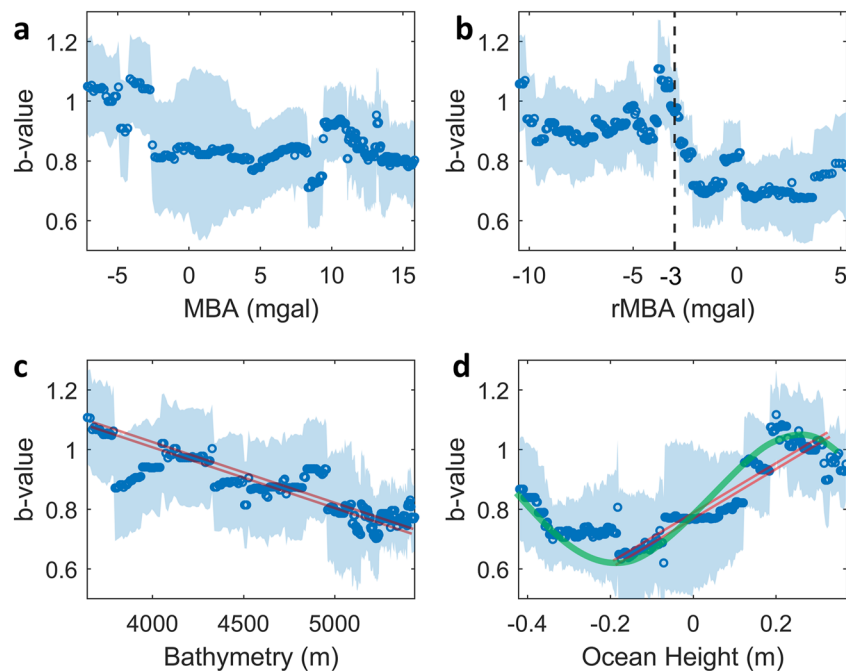


**Figure 5.** Single-parameter influence on magnitude distribution: (a) MBA (mgal), (b) rMBA (mgal), (c) bathymetry (m), and (d) ocean height (m). The blue dots show the  $b$ -values estimated by the repeated median technique for 100-event windows, plotted in the center of each window. The windows are shifted by 1 event after each calculation. The shaded areas show the bootstrap standard error of  $b$ -value estimation, derived by 1,000 resamplings. The vertical dashed line in (b) indicates the  $-3$  mgal threshold, dividing the data into high ( $<-3$  mgal) and low ( $>-3$  mgal)  $b$ -values, respectively. The red lines in (c) and (d) show average linear trends, whereas the green line in (d) indicates a sinusoidal approximation with peaks at approximately  $\pm 0.20$  m.

have larger  $b$ -values than event windows with  $rMBA > -3$  mgal. Division of data in two equally sized groups, suggests that events located at areas with  $rMBA < -3$  mgal have  $b = 1.04 \pm 0.13$ , and events located at areas with  $rMBA > -3$  mgal have  $b = 0.72 \pm 0.11$ . This  $b$ -value difference between the two datasets is statistically significant at 0.05 level (the  $t$ -statistic values is 1.96, Equation 5, Supporting Information S1). A relationship between magnitude distribution and bathymetry is indicated in Figure 5c, where  $b$ -values gradually decline with increasing ocean depth. The shallower depths are generally related to higher  $b$ -values in comparison to the areas with deeper bathymetry. If we divide the data into three evenly sized, nonoverlapping datasets, the resulting  $b$ -values are  $0.94 \pm 0.19$ ,  $0.86 \pm 0.17$ , and  $0.78 \pm 0.09$  for shallow, intermediate, and deep bathymetry, respectively. These values present considerable overlap with each other, and they clearly do not suggest a significant difference. However, they offer a rough view on the  $b$ -value distribution connected with bathymetry. A not so clear linear trend is observed in the tidal height plot (Figure 5d), with  $b$ -values seeming to monotonically increase for tidal heights between  $-0.2$  and  $0.2$  m. In general, earthquakes occurring at positive ocean heights (high tides) appear to demonstrate higher  $b$ -values than the ones that occur at negative ocean heights (low tides). A possible sinusoidal relation is also visible, although the uncertainties are too large to verify the significance of a sinusoidal shape.

Overall, our cluster analysis suggest that the eastern part of Chain at ELFS (Cluster 3/4) has remarkably different seismicity properties in comparison to the remaining TF, having high  $b$ -values and OBS seismicity rates, negative gravity anomalies, and shallow bathymetry (Figures 1, 3, and 4; Table 1). Cluster 1 (west part) and Cluster 2 (central part) have generally comparable parameter values and distribution and they cannot be clearly distinguished from each other. Only rMBA significantly influences  $b$ -values, while the other trends (MBA, bathymetry, tides) provide only indications of potential correlations.

### 3.2. Spatiotemporal Seismicity Variations From OBS and Historical Data

The average OBS seismicity rate is not equally distributed along the TF strike (Figure 6, Table 2). The first characteristic is that seismicity rates become higher from the west to the east, as suggested by the number of events

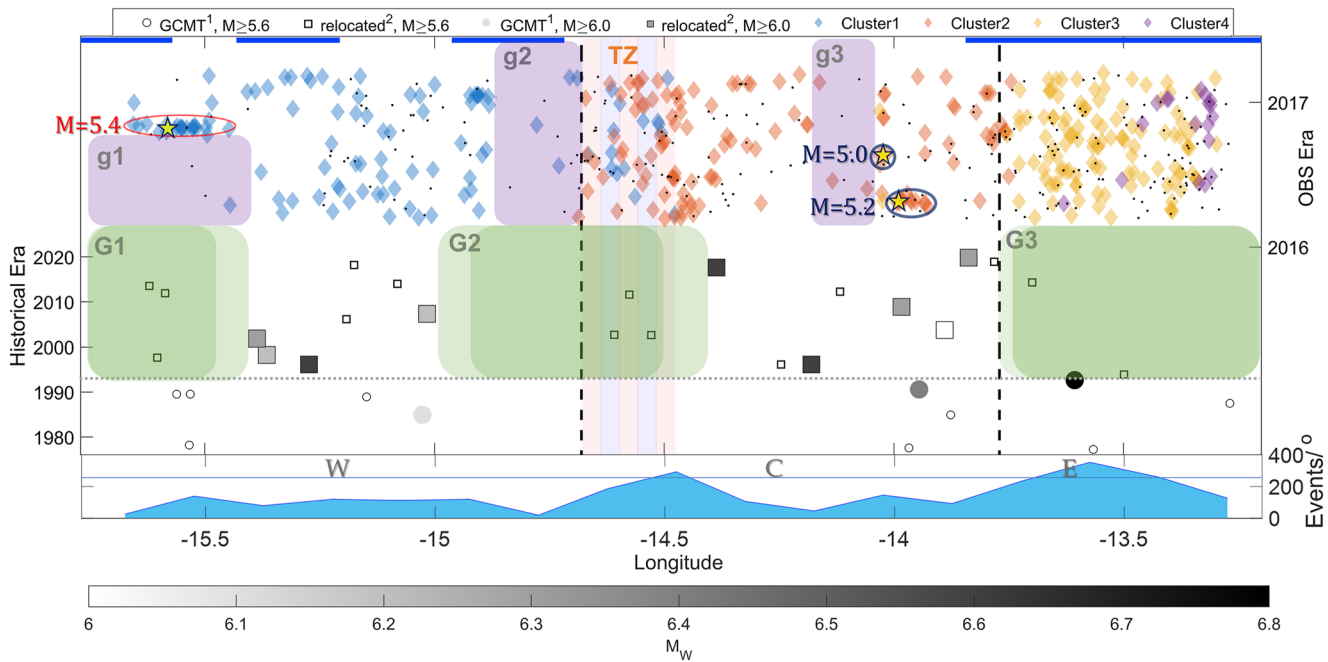


**Figure 6.** Longitude-date summation, integrating the data and results from ocean bottom seismometers (OBS) seismicity analysis (upper part, right y-axis) and global Centroid Moment Tensor (CMT) data (lower part, left y-axis). The four clusters in which OBS data were grouped are shown as colored diamonds (see legend for details) and comprise only the complete data with  $M_L \geq 2.3$ . The dots indicate the remaining microseismicity events with  $M_L < 2.3$ . The purple-shaded boxes denote the location of OBS seismicity gaps (g1, g2, g3). The transition zone (TZ) between Cluster 1 and Cluster 2 (see text for details) is shown by the colored vertical bars. Squares denote the relocated data from Shi et al. (2021) for events after 1993, whereas circles indicate the locations reported by International Seismological Center (ISC) for events before 1993. Gray-filled symbols represent the strongest ( $M_W \geq 6.0$ ) events that occurred since 1976, with the color scale beneath the plot indicating the magnitudes. Open symbols show the events with  $5.5 \leq M_W < 6.0$ . The light green boxes denote the location of historical seismicity gaps (G1, G2, G3), that is, areas with absence of  $M_W \geq 6.0$  events since 1993. The dark green boxes denote the historical seismicity gaps, considering half rupture length of the  $M > 6.0$  earthquakes after 1993. The temporal extent of the Shi et al. (2021) catalog (1993) is indicated by the dotted horizontal line. The blue horizontal lines just below the legend indicate the location of the flower structures. The dashed vertical lines divide Chain into three areas, Western (W), Central (C), and Eastern (E). The red and blue ellipses indicate the extent of the seismic activity related with the three strongest ( $M_L \geq 5.0$ ) events along Chain, which are marked by the yellow stars. The blue area at the bottom of the figure shows the moving mean OBS seismicity rate for nonoverlapping bins with  $0.15^\circ$  length.

per longitude degree (Table 2). The eastern area demonstrates three and two times higher activity rates compared to the central and western areas, respectively. There is a narrow Transition Zone (TZ in Figure 6) of  $\sim 25$  km, overlapping between Cluster 1 and Cluster 2, where there are 62 events (19 from Cluster 1 and 43 from Cluster 2). Cluster 1 is also defined by the existence of the three westernmost flower structures, and it contains fewer events in the transition zone. For these reasons we divided western and central areas at  $-14.68^\circ$  longitude. There

**Table 2**

*Summary of the Properties of Seismicity (From OBS and GCMT) in the Three Areas, as Derived by Multidimensional Cluster Analysis (Shown in Figure 3)*

	Western area	Central area	Eastern area
Longitude	$-15.65^\circ$ to $-14.68^\circ$	$-14.68^\circ$ to $-13.76^\circ$	$-13.76^\circ$ to $-13.29^\circ$
$N_{\text{obs}}/^\circ$ ( $M_L > 2.3$ )	98	148	296
$N_{\text{GCMT}}/^\circ$ ( $M_W \geq 5.5$ )	19.6	16.3	10.6
$b_{\text{OBS}}$	$0.89 \pm 0.12$	$0.74 \pm 0.13$	$0.98 \pm 0.15$
$b_{\text{merged}}$	$0.91 \pm 0.12$	$0.83 \pm 0.19$	$1.04 \pm 0.13$
$M_{0(\text{OBS})}/^\circ$	$1.88 \times 10^{17}$	$1.74 \times 10^{17}$	$0.64 \times 10^{17}$
$M_{0(\text{GCMT}_1993)}/^\circ$	$2.35 \times 10^{19}$	$3.47 \times 10^{19}$	$0.19 \times 10^{19}$

*Note.*  $N$  is the number of events,  $b$  is the GR law  $b$ -value, and  $M_0$  is the seismic moment. Apart from the  $b$ -values, all other parameters are normalized by longitude unit.

is also a very narrow zone between Cluster 2 and Cluster 3, including only three events from Cluster 3. For the same reasons, we divided central and eastern areas at  $-13.76^\circ$  longitude. There are three characteristic spatiotemporal OBS seismicity gaps (purple shaded zones, g1, g2, g3, Figure 6). OBS seismicity gaps are defined as areas where the seismicity rate drops below a specified level. We calculate the average OBS rate equal to 150 events ( $M_L \geq 2.3$ ) per longitude degree ( $^\circ$ ). We then define a seismicity gap when the rate falls below one-fifth of the average rate (30 events/ $^\circ$ ) for a length of at least  $0.15^\circ$  or  $\sim 15$  km (arbitrary selection). Gap g1 ( $\sim 40$  km length) is located at the same location as the westernmost flower structure and is characterized by an almost complete absence of events (three events, one above  $M_C = 2.3$ ) for at least 7 months before the occurrence of the October 27, 2016,  $M_L = 5.4$ , which was the strongest event recorded by the OBS network. Four events above  $M_C$  are found in gap g2 ( $\sim 20$  km length), which is located at the easternmost part of the western area. This gap overlaps substantially with the easternmost smaller flower structure in the western segment of the TF. Three events above  $M_C = 2.3$  occurred in gap g3 ( $\sim 15$  km length), which is located close to the middle of the central area. Gaps g2 and g3 persist for the entire duration of the OBS network.

The strongest  $M_W \geq 6$  events after 1993 (filled squares, Figure 6) are also not uniformly distributed. Four of them are located at the center of the western area, and five of them are located at the mid-eastern part of the central area. The existence of seismic gaps is shown for the historical data as the green shaded zones (G1, G2, G3, Figure 6). We define historical seismicity gaps as areas with lengths greater than 30 km, a length which could potentially rupture a roughly  $M_W = 6.6$  earthquake (Wells & Coppersmith, 1994), but where no events  $M_W \geq 6.0$  have been recorded since 1993. These gaps seem to be fairly stable even when we consider seismicity since 1976 (although uncertainties before 1993 are much higher). Gap G1 ( $\sim 40$  km length), coincides spatially with OBS seismicity gap g1, and is characterized by an episodic occurrence of events with  $5.6 \leq M_W < 6.0$ , approximately at the location of the October 27, 2016,  $M_L = 5.4$  event recorded by the OBS network. Two large gaps ( $\sim 65$  km length) are also present. Gap G2 occupies parts of the western and central areas. Only three events with  $5.6 \leq M_W < 6.0$  have occurred since 1993, whereas no  $M_W \geq 5.6$  has been recorded within over 40 km. Gap G3 essentially covers all the eastern area beneath the ELFS, where only two events with  $5.6 \leq M_W < 6.0$  have occurred since 1993. There is one strong event (1992,  $M_W = 6.8$ ) in the GCMT catalog, which has not been relocated, therefore there may be considerable location uncertainty. Comparison of the Shi et al. (2021) locations with ISC shows that the mean difference between the two is  $0.10^\circ$ , although there is one outlier  $0.70^\circ$  away (Figure S19 in Supporting Information S1). Therefore, it is likely that the event occurred in G3. In this case the segment would be characterized as relatively locked, with large magnitude earthquakes after long time periods. However, we cannot rule out the possibility that it occurred outside of G3, and in this case the segment would be characterized by weak coupling and creep.

It is worth noting that the gaps determined by the long-term data are not always consistent with the OBS seismicity gaps. Gaps in historical seismicity (G1, G2, G3), possibly represent patches that do not nucleate  $M \geq 6.0$  earthquakes. For the gaps in OBS seismicity (g1, g2, g3) there are three possible scenarios.

1. These gaps represent high coupling areas that potentially fail in future large earthquakes. In this case, gap g3 represents a highly locked area with fewer earthquakes, and it would be consistent with the long-term active segment between G2 and G3. In the case of g1, which coincides with the long-term G1, the observations favor this scenario as well, although the maximum magnitude of the events for the last 45 years in this area seems to be limited below  $M = 6.0$ . However, g2 would be inconsistent with this scenario since no  $M \geq 5.5$  historical events have occurred at these longitudes.
2. These gaps are creeping areas which generate smaller magnitude earthquakes (many of them possibly below the detection threshold of the OBS network). This case is consistent with the absence of seismic activity in g2 during both historical and OBS eras. However, this scenario would be inconsistent with the historical seismicity occurred at g3 and g1.
3. These gaps exhibit semi-brittle (multi-mode) behavior with time-dependent characteristics (Boettcher & Jordan, 2004).

Nearly all  $M_W \geq 6.0$  events occur at patches with moderate to small OBS seismicity rates (90–120 events/ $^\circ$ ) and the segments with the highest OBS seismic activity ( $>250$  events/ $^\circ$ ) are characterized as gaps (no events with  $M_W \geq 6.0$ ) by the long-term data (e.g., ELFS, central Chain) (Figure 6). Note that the historical seismicity gaps, defined by the centroid locations, indicate the upper bounds of these gaps (light green boxes, Figure 6). If we assume bilateral slip and extend the area that ruptured each  $M_W \geq 6.0$  by  $\sim 10$ – $15$  km (Wells & Coppersmith, 1994),

the dimensions of the gaps decrease but the general picture does not change significantly (dark green boxes in Figure 6). In that case the eastern border G2 would roughly coincide with the transition zone between Cluster 1 and Cluster 2 (i.e., west and central segments).

The  $b$ -value analysis resulting from the 1-year catalog may be artifacts arising from short sampling. For this reason, we carry out analysis for the merged catalog, to eliminate short-term biases. The  $b$ -values are generally consistent with each other when considering the OBS data alone and the merged catalog (Table 2). The central area (Cluster 2) demonstrates the lowest  $b$ -values ( $b \sim 0.70$ – $0.80$ ), although the difference from the other clusters is not statistically significant. The highest  $b$ -values are evident in the eastern area along the ELFS ( $b \sim 1.0$ ), where OBS seismicity rates are the highest. The three segments released the following proportions of seismic moment,  $M_0$ , in comparison to that released on Chain during the OBS deployment (normalized by longitude unit): western (44%), central (41%), and eastern (15%). When the merged catalog after 1993 is considered for events of  $M \geq 6.0$ , the proportion is as follows: western (39%), central (58%), and eastern (3%).

#### 4. Discussion

The generally low average  $b$ -values along Chain ( $\sim 0.85$ ) provide evidence of relatively high seismic coupling, defined as the area displaced by seismic slip divided by the thermally constrained seismogenic area. This agrees with estimates of theoretical versus observed seismic moment release which suggests that the seismic coupling coefficient in Chain equals  $\sim 1/3$  (Wolfson-Schwehr & Boettcher, 2019), which is among the highest values in the MAR (0.85 quantile).

There does not appear to be evidence for large repeating earthquakes along Chain TF. No  $M_w > 7.0$  events rupturing the entire TF have been recorded. No quasi-periodical earthquake cycle is evident for  $M_w \geq 6.0$  events along Chain for over 30 years. This is different from other transforms such as the Charlie-Gibbs TF (north Atlantic), which has strong earthquakes ( $M_w \sim 7.0$ ) that occur quasi-periodically (Aderhold & Abercrombie, 2016).

The lateral variability of frictional response is likely caused by some combination of the rock composition, stress/temperature conditions, fault geometry, and/or hydrothermal alteration (e.g., Liu et al., 2012; Roland et al., 2010, 2012; Wolfson-Schwehr et al., 2014). As mentioned earlier, the slow spread oceanic crust has a wide diversity of morphologies, with detachment faults and core complexes often associated with altered mantle material at the seafloor (Blackman et al., 1998). Deeper, in the oceanic mantle water can substantially weaken olivine (Kohli et al., 2021) by enhancing dislocation and diffusion creep mechanisms (Karato et al., 1986). It is also likely that the mafic crust contains pockets of serpentinite (barriers), resulting from tectonism or/and fluid flow through the fractured material (Gregory et al., 2021). Conversely, asperities may be caused by dry patches (inaccessible to water) or patches where there is an absence of serpentinite.

The historical teleseismic dataset indicates high lateral heterogeneity in seismicity along Chain. There is a long-term (1993–2021) absence of strong events within three gaps (G1, G2, G3, Figure 6). We observe two locked patches (asperities), with total length  $\sim 50$  and  $\sim 75$  km, respectively, which have repeatedly ruptured  $M_w > 6.0$  earthquakes (Figure 6). Lateral heterogeneity is also inferred from the OBS data. The gaps in OBS seismicity (g1, g2, g3, Figure 6) do not necessarily occur in the same locations at those in the historical records, although areas with intermediate to low OBS seismicity rates ( $\sim 100$  events/ $^\circ$ ) occur in regions where teleseismic  $M_w > 6.0$  earthquakes tend to occur. For comparison, the average OBS activity rate along Chain is 150 events/ $^\circ$  (see also Table 2 and Figure 6). The observed transform segmentation along Chain (three areas) is in general agreement with the conceptual models of Boettcher and Jordan (2004). In these models the seismogenic zone is divided into multiple patches, such that either brittle (purely coupled), ductile (purely aseismic), or time-dependent (semi-brittle) deformation applies. The eastern area is characterized by the presence of ELFS, negative rMBA, abundant OBS seismicity, but negligible seismic moment release, evidenced by the historical data. Negative rMBA areas are explained by mass deficit, likely caused by thicker crust and/or hydrothermal alteration (T. Wang et al., 2011). This area is also accompanied by higher  $b$ -values, consistent with weaker coupling (i.e., less brittle behavior). The negative rMBA combined with the shallowest bathymetry occurring beneath at ELFS, likely suggests that the crust is either thicker by up to 1 km or has an altered crust and/or mantle with lower densities (Harmon et al., 2018). The abundant but low magnitude seismicity is more consistent with low density altered material, and this is our preferred interpretation. However, we cannot preclude the possibility that the crust is also a bit thicker.



In contrast to the ELFS, the western and central areas exhibit positive rMBA, lower OBS seismicity rates (three and two times lower than the eastern area, respectively), but they accommodate almost the entire long-term moment released seismically, by  $M \geq 6.0$  historical events along Chain (>97%). Positive rMBA anomalies require mass excesses. This can be explained by thinned crust and/or a lack of hydrothermal alteration (T. Wang et al., 2011). These regions are also associated with lower  $b$ -values, indicative of greater coupling and more brittle behavior. It seems that there are other physical mechanisms controlling the distribution of small and large earthquakes along the western and central segments that are not sufficiently captured by the selected set of parameters. Although the western segment exhibits flower structures similar to ELFS, the degree of alteration is not as strong, possibly owing to their smaller size or temporal variations.

Three  $5.0 \leq M_L \leq 5.4$  earthquakes were recorded by the OBS network along the Chain TF. The April 27, 2016,  $M_L = 5.2$ , was preceded by eight  $M_L \geq 2.3$  events in the week before and was followed by three  $M_L \geq 2.3$  events in the week after the main shock occurrence. The August 20, 2016,  $M_L = 5.0$  earthquake had no precursors in the week before and was followed by three  $M_L \geq 2.3$  events in the week after the main shock occurrence. These two mainshocks had similar size and occurred at the western tip of the eastern area at approximately the same location (Figure 6, Figure S20 in Supporting Information S1). However, they demonstrate diverse foreshock activity and a negligible aftershock sequence. The October 27, 2016,  $M_L = 5.4$  event was preceded by only two, yet relatively strong events ( $M_L \geq 4.0$ ) in the week before and was followed by 13  $M_L \geq 2.3$  events in the week after the main shock occurrence, indicating a rather weak mainshock-aftershock sequence. These cases agree with the notion that mainshock-aftershock sequences are not common for oceanic TF earthquakes (e.g., Scholz, 2019). Our results are also consistent with the global perspective, showing that the number of aftershocks at oceanic TF are typically  $\sim 1$  order of magnitude fewer than continental earthquakes, possibly due to the much slower rate of static fatigue of gabbro compared to granite (Meredith & Atkinson, 1985) and the existence of serpentine phases. High numbers of foreshocks have been mainly observed in segments of the East Pacific Rise, where they have been successfully used for retrospective prediction of  $M \geq 5.4$  events (McGuire et al., 2005). McGuire (2003) detected no foreshocks (within 1 hr and 20 km from the mainshock) in various TFs along MAR and Juan de Fuca (intermediate slip rate). We also found no foreshocks with such criteria for the OBS  $M \geq 5.0$  events.

Two out of three possible frictional scenarios suggest that OBS seismicity gaps are either highly coupled patches (potentially producing  $M > 5.5$  earthquakes) or creeping areas that generate microseismicity. The third scenario, semi-brittle behavior, is related with temporal frictional changes. Such behavior cannot be excluded and has been suggested for slow slipping TFs (e.g., Aderhold & Abercrombie, 2016), although global observations show that it is rather rare (Shi et al., 2021). Semi-brittle behavior may be caused by the temporal changes in pore pressure due to fluid circulation, leading to subsequent draining and fluid saturation stages as well as to periodic hydration and dehydration of peridotite. Both effects can switch the rupture mode between seismic and aseismic slip depending on whether a positive or a negative feedback loop is activated (e.g., Renard, 2021). 3D rate/state friction models suggest that TF segments switch between seismic and aseismic slip over many earthquake cycles (Liu et al., 2012). Time-dependent features are also supported by analysis of exhumed ancient oceanic TF rock samples (Cox et al., 2021). Note that a characteristic property of serpentine is that, depending upon the applied strain rate it may demonstrate both seismic (frictional decrease under fast loading velocities) and aseismic (frictional increase under slow loading velocities) behavior. Thus, both stable and unstable slip propagation is plausible in the presence of serpentinized rocks (Reinen et al., 1991).

## 5. Conclusions

We investigate the seismotectonic properties along Chain TF at the equatorial MAR by combining geophysical data with a  $\sim 1$ -year OBS seismicity data and 30-year historical earthquake data. Our analysis shows that Chain can be divided into three segments: west, central, and east. We find that OBS seismicity occurs at much higher rates at the east part of Chain ( $\sim 300$  events/°), co-located with the largest flower structure (transpressional morphological feature) and negative rMBA values. The majority of seismic moment is released at the west and central areas with much less moment release in the east area, as inferred from both OBS and historical data. OBS seismicity rates in a given area are not always directly related to the presence or absence of large historical earthquakes. However, the patches with the highest OBS seismicity rates have not hosted  $M_w \geq 6.0$  events. There are two 50–75 km long segments (asperities) with moderate to low OBS seismicity rates ( $\sim 100$  events/°), occasionally hosting  $M_w \geq 6.0$  earthquakes. These two segments are separated by three 40–65 km long historical

seismicity gaps, with few historical earthquakes with  $5.5 \leq M_w < 6.0$ , but generally high OBS seismicity ( $>200$  events/°). We find higher  $b$ -values in locations of lower rMBA and shallower bathymetry, likely indicative of thickened crust and/or low density (altered) mantle. The existence of seismic/aseismic patches and the differences between aseismic/seismic behavior in OBS versus historical earthquakes imply heterogeneity along the fault, possibly due to variable hydrothermal circulation/alteration. Our results also suggest that earthquake occurrence rates and size in a given location can be variable in time. These variations are likely dictated by lateral variations between regions characterized by hydrothermal alteration (barriers) and normal gabbroic crust/unaltered mantle lithosphere (asperities).

## Data Availability Statement

The seismic data are archived at the IRIS DMC, as 2016–2017 network XS [https://doi.org/10.7914/SN/XS\\_2016](https://doi.org/10.7914/SN/XS_2016) (Rychert et al., 2016). The earthquake catalog used in the study is available as a pre-print from Schlaphorst et al. (2022, <https://doi.org/10.1002/essoar.10511147.1>). The global seismicity data come from GCMT, [www.globalcmt.org/](http://www.globalcmt.org/), last accessed March 2022. The relocated data come from Shi et al. (2021), available at <https://doi.org/10.5281/zenodo.4646438>, last accessed June 2021. Figure 1 was generated using Generic Mapping Tools v.6.1.1 ([www.soest.hawaii.edu/gmt](http://www.soest.hawaii.edu/gmt), last accessed March 2022). Most of the analysis and figures were done by MATLAB (The MathWorks®, 2021b, Natick, USA). The MATLAB codes for the Transformation to Equivalent Dimensions, Cluster Analysis, and Anderson-Darling test can be downloaded from <https://git.plgrid.pl/projects/EA/repos/sera-applications/browse/>, last accessed March 2022. On-line versions of the software are available in the Thematic Core Service – Anthropogenic Hazards web platform (<https://tcs.ah-epos.eu/>; Orlecka-Sikora et al., 2020; Leptokaropoulos et al., 2019).

## Acknowledgments

K. Leptokaropoulos, C. A. Rychert, and N. Harmon acknowledge funding from the Natural Environment Research Council (NE/M003507/1) and the European Research Council (GA 638665). J. M. Kendall was funded by the Natural Environment Research Council (NE/M004643/1). We thank the captain and crew of the R/V Marcus G. Langseth and the RRS Discovery, and the scientific technicians. We thank David Schlaphorst for discussions on magnitudes and focal mechanisms calculation. We thank Jochen Braunmiller and an anonymous reviewer, the Associate Editor, and Editor, Satoshi Ide, for their insightful comments and suggestions.

## References

- Abercrombie, R. E., & Ekström, G. (2001). Earthquake slip on oceanic transform faults. *Nature*, 410(6824), 74–77. <https://doi.org/10.1038/35065064>
- Aderhold, K., & Abercrombie, R. E. (2016). The 2015 Mw 7.1 earthquake on the Charlie-Gibbs transform fault: Repeating earthquakes and multimodal slip on a slow oceanic transform. *Geophysical Research Letters*, 43(12), 6119–6128. <https://doi.org/10.1002/2016GL068802>
- Agius, M. R., Harmon, N., Rychert, C. A., Tharimena, S., & Kendall, J. M. (2018). Sediment characterization at the equatorial Mid-Atlantic Ridge from P-to-S teleseismic phase conversions recorded on the PI-LAB experiment. *Geophysical Research Letters*, 45(22), 12244–12252. <https://doi.org/10.1029/2018GL080565>
- Agius, M. R., Rychert, C. A., Harmon, N., Tharimena, S., & Kendall, J. M. (2021). A thin mantle transition zone beneath the equatorial Mid-Atlantic Ridge. *Nature*, 589(7843), 562–566. <https://doi.org/10.1038/s41586-020-03139-x>
- Agnew, D. C. (1997). NLOADF: A program for computing ocean-tide loading. *Journal of Geophysical Research*, 102(B3), 5109–5110. <https://doi.org/10.1029/96jb03458>
- Amorè, D., Grasso, J.-R., & Rydelek, P. A. (2010). On varying  $b$  values with depth: Results from computer-intensive tests for southern California. *Geophysical Journal International*, 180(1), 347–360. <https://doi.org/10.1111/j.1365-246X.2009.04414.x>
- Behn, M. D., Boettcher, M. S., & Hirth, G. (2007). Thermal structure of oceanic transform faults. *Geology*, 35(4), 307–310. <https://doi.org/10.1130/G23112A.1>
- Blackman, D. K., Cann, J. R., Janssen, B., & Smith, D. K. (1998). Origin of extensional core complexes: Evidence from the Mid-Atlantic Ridge at Atlantis Fracture Zone. *Journal of Geophysical Research*, 103(B9), 21315–21333. <https://doi.org/10.1029/98jb01756>
- Boettcher, M. S., & Jordan, T. H. (2004). Earthquake scaling relations for mid-ocean ridge transform faults. *Journal of Geophysical Research*, 109(B12), B12302. <https://doi.org/10.1029/2004JB003110>
- Boettcher, M. S., & McGuire, J. J. (2009). Scaling relations for seismic cycles on mid-ocean ridge transform faults. *Geophysical Research Letters*, 36(21), L21301. <https://doi.org/10.1029/2009GL040115>
- Bogiatzis, P., Karamitrou, A., Ward Neale, J., Harmon, N., Rychert, C. A., & Srokosz, M. (2020). Source regions of infragravity waves recorded at the bottom of the equatorial Atlantic Ocean, using OBS of the PI-LAB experiment. *Journal of Geophysical Research: Oceans*, 125(6), e2019JC015430. <https://doi.org/10.1029/2019JC015430>
- Braunmiller, J., & Nabelek, J. (2008). Segmentation of the Blanco Transform Fault Zone from earthquake analysis: Complex tectonics of an oceanic transform fault. *Journal of Geophysical Research*, 113(B7), B07108. <https://doi.org/10.1029/2007jb005213>
- Brune, J. N. (1968). Seismic moment, seismicity, and rate of slip along major fault zones. *Journal of Geophysical Research*, 73(2), 777–784. <https://doi.org/10.1029/jb073i002p00777>
- Cox, S., Fagereng, A., & MacLeod, C. J. (2021). Shear zone development in serpentinized mantle: Implications for the strength of oceanic transform faults. *Journal of Geophysical Research: Solid Earth*, 126(5), e2020JB020763. <https://doi.org/10.1029/2020jb020763>
- Egbert, G. D., & Erofeeva, S. Y. (2002). Efficient inverse modeling of barotropic ocean tides. *Journal of Atmospheric and Oceanic Technology*, 19(2), 183–204. [https://doi.org/10.1175/1520-0426\(2002\)019<0183:eimob>2.0.co;2](https://doi.org/10.1175/1520-0426(2002)019<0183:eimob>2.0.co;2)
- Ekström, G., Nettles, M., & Dziewoński, A. (2012). The global CMT project 2004–2010: Centroid-moment tensors for 13,017 earthquakes. *Physics of the Earth and Planetary Interiors*, 200–201, 1–9. <https://doi.org/10.1016/j.pepi.2012.04.002>
- Engeln, J. F., Wiens, D. A., & Stein, S. (1986). Mechanisms and depths of Atlantic transform earthquakes. *Journal of Geophysical Research*, 91(B1), 548–577. <https://doi.org/10.1029/jb091ib01p00548>
- Fischer, K. M., Ford, H. L., Abt, D. L., & Rychert, C. A. (2010). The lithosphere-asthenosphere boundary. *Annual Review of Earth and Planetary Sciences*, 38(1), 551–575. <https://doi.org/10.1146/annurev-earth-040809-152438>
- Fischer, K. M., Rychert, C. A., Dalton, C., Miller, M., Beghein, C., & Schutt, D. (2020). A comparison of oceanic and continental mantle lithosphere. *Physics of the Earth and Planetary Interiors*, 309, 106600. <https://doi.org/10.1016/j.pepi.2020.106600>

- Froment, B., McGuire, J. J., van der Hilst, R. D., Gouedard, P., Roland, E. C., Zhang, H., & Collins, J. A. (2014). Imaging along-strike variations in mechanical properties of the Gofar transform fault, East Pacific Rise. *Journal of Geophysical Research: Solid Earth*, 119(9), 7175–7194. <https://doi.org/10.1002/2014jb011270>
- Gregory, E. P. M., Singh, S. C., Marjanović, M., & Wang, Z. (2021). Serpentinized peridotite versus thick mafic crust at the Romanche oceanic transform fault. *Geology*, 49(9), 1132–1136. <https://doi.org/10.1130/G49097.1>
- Hanks, T. C., & Kanamori, H. (1979). A moment magnitude scale. *Journal of Geophysical Research*, 84(B5), 2348–2350. <https://doi.org/10.1029/jb084ib05p02348>
- Harding, T. P. (1985). Seismic characteristics and identification of negative flower structures, positive flower structures, and positive structural inversion. *AAPG Bulletin*, 69, 585–600.
- Harmon, N., Laske, G., Crawford, W., & Rychert, C. A. (2022). Tilt corrections for normal mode observations on ocean bottom seismic data, an example from the PI-LAB experiment. *Seismica*, 1(1). <https://doi.org/10.26434/seismica.v1i1.196>
- Harmon, N., Rychert, C. A., Agius, M., Tharimena, S., Le Bas, T., Kendall, J. M., & Constable, S. (2018). Marine geophysical investigation of the Chain fracture zone in the equatorial Atlantic from the PI-LAB experiment. *Journal of Geophysical Research: Solid Earth*, 123(12), 11016–11030. <https://doi.org/10.1029/2018JB015982>
- Harmon, N., Rychert, C. A., Michael Kendall, J., Agius, M., Bogiatzis, P., & Tharimena, S. (2020). Evolution of the oceanic lithosphere in the equatorial Atlantic from Rayleigh Wave tomography, evidence for small-scale convection from the PI-LAB experiment. *Geochemistry, Geophysics, Geosystems*, 21(9), e2020GC009174. <https://doi.org/10.1029/2020GC009174>
- Harmon, N., Wang, S., Rychert, C. A., Constable, S., & Kendall, J. M. (2021). Shear velocity inversion guided by resistivity structure from the PI-LAB experiment for integrated estimates of partial melt in the mantle. *Journal of Geophysical Research*, 126(8), e2021JB022202. <https://doi.org/10.1029/2021JB022202>
- Hensen, C., Duarte, J. C., Vannucchi, P., Mazzini, A., Lever, M. A., Terrinha, P., et al. (2019). Marine transform faults and fracture zones: A joint perspective integrating seismicity, fluid flow and life. *Frontiers of Earth Science*, 7, 39. <https://doi.org/10.3389/feart.2019.00039>
- Hicks, S. P., Okuwaki, R., Steinberg, A., Rychert, C. A., Harmon, N., Abercrombie, R., et al. (2020). Back-propagating supershear rupture in the 2016 Mw 7.1 Romanche transform fault earthquake. *Nature Geoscience*, 13(9), 647–653. <https://doi.org/10.1038/s41561-020-0619-9>
- Karato, S.-I., Paterson, M., & Fitzgerald, D. (1986). Rheology of synthetic olivine aggregates: Influence of grain size and water. *Journal of Geophysical Research*, 91, 8151–8176.
- Kohl, A., Wolfson-Schwehr, M., Prigent, C., & Warren, J. M. (2021). Oceanic transform fault seismicity and slip mode influenced by seawater infiltration. *Nature Geoscience*, 14(8), 606–611. <https://doi.org/10.1038/s41561-021-00778-1>
- Kuna, V. M., Nabělek, J. L., & Braunmiller, J. (2019). Mode of slip and crust–mantle interaction at oceanic transform faults. *Nature Geoscience*, 12(2), 138–142. <https://doi.org/10.1038/s41561-018-0287-1>
- Lasocki, S. (2014). Transformation to equivalent dimension – A new methodology to study earthquake clustering. *Geophysical Journal International*, 197(2), 1224–1235. <https://doi.org/10.1093/gji/ggu062>
- Leptokaropoulos, K. (2020). Magnitude distribution complexity and variation at the Geysers geothermal field. *Geophysical Journal International*, 222(2), 893–906. <https://doi.org/10.1093/gji/ggaa208>
- Leptokaropoulos, K., Cielesta, S., Staszek, M., Olszewska, D., Lizurek, G., Kocot, J., et al. (2019). IS-EPOS: A platform for anthropogenic seismicity research. *Acta Geophysica*, 67(1), 299–310. <https://doi.org/10.1007/s11600-018-0209-z>
- Leptokaropoulos, K., Harmon, N., Hicks, S., Rychert, C. A., Schlaphorst, D., & Kendall, J. M. (2021). Tidal triggering of microseismicity at the equatorial Mid-Atlantic Ridge, inferred from the PI-LAB experiment. *Journal of Geophysical Research: Solid Earth*, 126(9), e2021JB022251. <https://doi.org/10.1029/2021JB022251>
- Liu, Y., McGuire, J. J., & Behn, M. D. (2012). Frictional behavior of oceanic transform faults and its influence on earthquake characteristics. *Journal of Geophysical Research*, 117(B4), B04315. <https://doi.org/10.1029/2011jb009025>
- Marjanović, M., Singh, S. C., Gregory, E. P. M., Grevemeyer, I., Growe, K., Wang, Z., et al. (2020). Seismic crustal structure and morphotectonic features associated with the Chain Fracture Zone and their role in the evolution of the equatorial Atlantic region. *Journal of Geophysical Research: Solid Earth*, 125(10), e2020JB020275. <https://doi.org/10.1029/2020JB020275>
- Marsaglia, G., & Marsaglia, J. (2004). Evaluating the Anderson-Darling distribution. *Journal of Statistical Software*, 9(2), 1–5. <https://doi.org/10.18637/jss.v009.i02>
- McGuire, J. J. (2003). Immediate foreshock sequences of oceanic transform earthquakes on the East Pacific Rise. *Bulletin of the Seismological Society of America*, 93(2), 948–952. <https://doi.org/10.1785/0120020151>
- McGuire, J. J., Boettcher, M. S., & Jordan, T. H. (2005). Foreshock sequences and short-term earthquake predictability on East Pacific Rise transform faults. *Nature*, 434(7032), 457–461. <https://doi.org/10.1038/nature03377>
- McGuire, J. J., Collins, J. A., Gouedard, P., Roland, E., Lizarralde, D., Boettcher, M. S., et al. (2012). Variations in earthquake rupture properties along the Gofar transform fault, East Pacific Rise. *Nature Geoscience*, 5, 336–341. <https://doi.org/10.1038/ngeo1454>
- Meredith, P. G., & Atkinson, B. K. (1985). Fracture toughness and subcritical crack growth during high temperature tensile deformation of westerly granite and black gabbro. *Physics of the Earth and Planetary Interiors*, 39(1), 33–51. [https://doi.org/10.1016/0031-9201\(85\)90113-x](https://doi.org/10.1016/0031-9201(85)90113-x)
- Molnar, P. (2020). The brittle-plastic transition, earthquakes, temperatures, and strain rates. *Journal of Geophysical Research: Solid Earth*, 125(7), e2019JB019335. <https://doi.org/10.1029/2019JB019335>
- Orlecka-Sikora, B., Lasocki, S., Kocot, J., Szeplieniec, T., Grasso, J. R., Garcia, A., et al. (2020). An open data infrastructure for the study of anthropogenic hazards linked to georesource exploitation. *Scientific Data*, 7(1), 89. <https://doi.org/10.1038/s41597-020-0429-3>
- Pan, J., Antolik, M., & Dziewonski, A. M. (2002). Locations of mid-oceanic earthquakes constrained by seafloor bathymetry. *Journal of Geophysical Research*, 107(B11), EPM 8-1–EPM 8-13. <https://doi.org/10.1029/2001JB001588>
- Reinen, L. A., Weeks, J. D., & Tullis, T. E. (1991). The frictional behavior of serpentinite: Implications for aseismic creep. *Geophysical Research Letters*, 18(10), 1921–1924. <https://doi.org/10.1029/91GL02367>
- Renard, F. (2021). Reaction-induced fracturing: When chemistry breaks rocks. *Journal of Geophysical Research: Solid Earth*, 126(2), e2020JB021451. <https://doi.org/10.1029/2020jb021451>
- Roland, E., Behn, M. D., & Hirth, G. (2010). Thermal-mechanical behavior of oceanic transform faults: Implications for the spatial distribution of seismicity. *Geochemistry, Geophysics, Geosystems*, 11(7), Q07001. <https://doi.org/10.1029/2010GC003034>
- Roland, E., Lizarralde, D., McGuire, J. J., & Collins, J. A. (2012). Seismic velocity constraints on the material properties that control earthquake behavior at the Quebrada-Discovery-Gofar transform faults, East Pacific Rise. *Journal of Geophysical Research*, 117(B11), B11102. <https://doi.org/10.1029/2012jb009422>
- Rychert, C., Kendall, J. M., & Harmon, N. (2016). Passive imaging of the lithosphere-asthenosphere boundary [Dataset]. International Federation of Digital Seismograph Networks. [https://doi.org/10.7914/SN/XS\\_2016](https://doi.org/10.7914/SN/XS_2016)

- Rychert, C. A., Harmon, N., Constable, S., & Wang, S. (2020). The nature of the lithosphere–asthenosphere boundary. *Journal of Geophysical Research: Solid Earth*, 125(10), e2018JB016463. <https://doi.org/10.1029/2018JB016463>
- Rychert, C. A., Tharimena, S., Harmon, N., Wang, S., Constable, S., Kendall, J. M., et al. (2021). A dynamic lithosphere–asthenosphere boundary near the equatorial Mid-Atlantic Ridge. *Earth and Planetary Science Letters*, 566, 116949. <https://doi.org/10.1016/j.epsl.2021.116949>
- Saikia, U., Rychert, C., Harmon, N., & Kendall, J. M. (2020). Sediment structure at the equatorial mid-atlantic ridge constrained by seafloor admittance using data from the PI-LAB experiment. *Marine Geophysical Research*, 41(1), 3. <https://doi.org/10.1007/s11001-020-09402-0>
- Saikia, U., Rychert, C., Harmon, N., & Kendall, J. M. (2021a). Seismic attenuation at the equatorial Mid-Atlantic Ridge constrained by local Rayleigh wave analysis from the PI-LAB experiment. *Geochemistry, Geophysics, Geosystems*, 22, e2021GC010085. <https://doi.org/10.1029/2021GC010085>
- Saikia, U., Rychert, C., Harmon, N., & Kendall, J. M. (2021b). Upper mantle anisotropic shear velocity structure at the equatorial Mid-Atlantic ridge constrained by Rayleigh wave group velocity analysis from the PI-LAB experiment. *Geochemistry, Geophysics, Geosystems*, 22, e2020GC009495. <https://doi.org/10.1029/2020GC009495>
- Schlaphorst, D., Rychert, C., Harmon, N., Hicks, S., Bogiatzis, P., Kendall, J. M., & Abercrombie, R. (2022). Local seismicity around the Chain Transform Fault at the Mid-Atlantic Ridge from OBS observations. *Geophysical Journal International*. Preprint submitted. <https://doi.org/10.1002/essoar.10511147.1>
- Scholz, C. (2019). *The mechanics of earthquakes and faulting* (3rd ed.). Cambridge University Press. <https://doi.org/10.1017/9781316681473>
- Shi, P., Meng, W., & Pockalny, R. (2021). The ubiquitous creeping segments on oceanic transform faults. *Geology*, 50(2), 199–204. <https://doi.org/10.1130/G49562.1>
- Silverman, B. W. (1986). *Density estimation for statistics and data analysis*, Monograph (p. 175). CRC Press.
- Wang, S., Constable, S., Reyes-Ortega, V., & Rychert, C. A. (2019). A marine magnetotelluric coast effect sensitive to the lithosphere–asthenosphere boundary. *Geophysical Journal International*, 218(2), 978–987. <https://doi.org/10.1093/gji/ggz202>
- Wang, S., Constable, S., Rychert, C. A., & Harmon, N. (2020). A lithosphere–asthenosphere boundary and partial melt estimated using marine magnetotelluric data at the central Middle Atlantic Ridge. *Geochemistry, Geophysics, Geosystems*, 21(9), e2020GC009177. <https://doi.org/10.1029/2020GC009177>
- Wang, T., Lin, J., Tucholke, B., & Chen, Y. J. (2011). Crustal thickness anomalies in the North Atlantic Ocean basin from gravity analysis. *Geochemistry, Geophysics, Geosystems*, 12(3). <https://doi.org/10.1029/2010GC003402>
- Ward, J. H. (1963). Hierarchical grouping to optimize an objective function. *Journal of the American Statistical Association*, 58(301), 236–244. <https://doi.org/10.1080/01621459.1963.10500845>
- Wells, D. L., & Coppersmith, K. J. (1994). New empirical relationships among magnitude, rupture length, rupture width, rupture area, and surface displacement. *Bulletin of the Seismological Society of America*, 84, 974–1002.
- Wolfson-Schwehr, M., & Boettcher, M. S. (2019). Chapter 2 – Global characteristics of oceanic transform fault structure and seismicity. In J. C. Duarte (Ed.), *Transform plate boundaries and fracture zones* (pp. 21–59). Elsevier. <https://doi.org/10.1016/B978-0-12-812064-4.00002-5>
- Wolfson-Schwehr, M., Boettcher, M. S., McGuire, J. J., & Collins, J. A. (2014). The relationship between seismicity and fault structure on the Discovery transform fault, East Pacific Rise. *Geochemistry, Geophysics, Geosystems*, 15(9), 3698–3712. <https://doi.org/10.1002/2014GC005445>

## References From the Supporting Information

- Aki, K. (1965). Maximum likelihood estimate of  $b$  in the formula  $\log N = a - bM$  and its confidence limits. *Bulletin of Earthquake Research Institute of the University of Tokyo*, 43, 237–239.
- Leptokaropoulos, K., Karakostas, V., Papadimitriou, E., Adamaki, A., Tan, O., & İnan, S. (2013). A homogeneous earthquake catalog for Western Turkey and magnitude of completeness determination. *Bulletin of the Seismological Society of America*, 103(5), 2739–2751. <https://doi.org/10.1785/0120120174>
- Schuster, A. (1897). On lunar and solar periodicities of earthquakes. *Proceedings of the Royal Society of London*, 61, 455–465. <https://doi.org/10.1098/rspl.1897.0060>
- Siegel, A. F. (1982). Robust regression using repeated medians. *Biometrika*, 69(1), 242–244. <https://doi.org/10.1093/biomet/69.1.242>
- Wiemer, S., & Wyss, M. (2000). Minimum magnitude of completeness in earthquake catalogs: Examples from Alaska, the Western United States, and Japan. *Bulletin of the Seismological Society of America*, 90(4), 859–886. <https://doi.org/10.1785/0119990114>